Ocean Engineering 294 (2024) 116862

Contents lists available at ScienceDirect

Ocean Engineering

journal homepage: www.elsevier.com/locate/oceaneng

Joint multi-objective optimization based on multitask and multi-fidelity Gaussian processes for flapping foil

Zhangyuan Wang [a,b], Yuqi Yan [b], Xinyu Zeng [c], Ruipeng Li [b,e,*], Weicheng Cui [b,e], Youzhi Liang [d], Dixia Fan [b,e]

[a] Zhejiang University-Westlake University Joint Training, Zhejiang University, Hangzhou, China
[b] Key Laboratory of Coastal Environment and Resources of Zhejiang Province, School of Engineering, Westlake University, Hangzhou, China
[c] Institute of Computer Technologies, Automation and Metrology, Lviv Polytechnic National University, Lviv, Ukraine
[d] Computer Science Department, Stanford University, Stanford, USA
[e] Institute of Advanced Technology, Westlake Institute for Advanced Study, Hangzhou, China

ARTICLE INFO

Keywords:
Multi-objective optimization
Multitask and multi-fidelity Gaussian processes
Bi-level genetic algorithm
Flapping foil

ABSTRACT

Focusing on the optimization of flapping foil geometry and motion parameters, this study proposes a joint multi-objective optimization strategy based on the multitask and multi-fidelity Gaussian process (MMGP). A multi-objective expected improvement (MOEI) acquisition function is first introduced and applied, treating the exploration and the exploitation as independent objectives. By using the ZDT1 test function, the MOEI method is verified to be better than the conventional weighted EI method in terms of prediction accuracy. Upon the establishment of the model, the correlation and sensitivity analyses are carried out based on the data set. Subsequently, this methodology is utilized to execute a joint optimization of geometry and motion parameters across different fidelity levels, aiming to attain global optimal solutions. To boost the optimization outcomes, a bi-level genetic algorithm (BiGA) is further designed and implemented, through which an configuration optimization for the amphibious foil considering multiple motion modalities is accomplished. This study not only presents a theoretical foundation for optimizing the design of the flapping foil but also offers effective strategies and methods for practical implementation.

1. Introduction

Flapping foils are bio-inspired devices that can generate thrust and lift by mimicking the motion of some kinds of aquatic and aerial animals. Many animals in nature have achieved amphibious capabilities by flapping their wings or fins, such as flying fish, seagulls, and cormorants (Wang et al., 2020; Zhang et al., 2019). Consequently, the concept of flapping foils holds significant potential in the creation of amphibious robots, engineered to operate seamlessly in both air and water (Wu et al., 2020; Wang et al., 2020; Zhang et al., 2019). However, the endeavor of designing and optimizing an efficient and versatile amphibious foil is an intricate challenge due to the different performance objectives and constraints in different media. For example, aerial flapping foils need to generate substantial lift, while underwater flapping foils must prioritize the production of enhanced thrust (Wang et al., 2020; Schouveiler et al., 2005).

With the rapid development of artificial intelligence (AI), more and more AI algorithms have been applied to the optimization of flapping foils or amphibious robots, providing new approaches and solutions for improving their performance and versatility. For example, surrogate models based on machine learning techniques can reduce the computational cost and improve the accuracy of optimization algorithms by learning from data and approximating the objective functions (Alizadeh et al., 2020). Genetic algorithms (GA) are a class of evolutionary algorithms that can explore a large and complex search space by mimicking the natural selection and genetic variation processes (Singh et al., 2018). These methods have been shown to be effective in optimizing the geometry or motion parameters of flapping foils for different objectives such as thrust, lift, efficiency, or maneuverability (Licht et al., 2009; Tuncer and Kaya, 2005; Zheng et al., 2020; Zhang et al., 2022; Ji et al., 2022).

There have been some representative works that employ AI methods to optimize amphibious robots and flapping foils. A comprehensive review by Sun et al. (2022) categorizes bio-inspired fish robots based on their mechanical properties, such as rigid, flexible, soft, and amphibious

* Corresponding author at: Key Laboratory of Coastal Environment and Resources of Zhejiang Province, School of Engineering, Westlake University, Hangzhou, China.
E-mail address: liruipeng@westlake.edu.cn (R. Li).

https://doi.org/10.1016/j.oceaneng.2024.116862
Received 19 September 2023; Received in revised form 25 December 2023; Accepted 22 January 2024

types. In the realm of propulsion optimization, Wang et al. (2020) and Schouveiler et al. (2005) employ genetic algorithms and particle swarm optimization, respectively. For path planning, Li and Wang (2021) introduces a fireworks algorithm-based approach, taking into account distance, energy consumption, and mode-switching costs, an aspect further explored in the turtle-inspired robot by Zheng et al. (2022). Notably, Licht et al. (2009) investigates the asymmetric flapping motion inspired by sea turtles, expanding the applicability to both aquatic and aerial environments.

Although these studies have utilized various optimization methods such as genetic algorithms, the particle swarm optimization, and fireworks algorithms. To the best of our knowledge, we have not seen anyone focused on both the geometry and the motion parameters for amphibious robots. The BiGA is a specialized genetic algorithm designed to solve nested optimization problems with interacting decision-making units at different hierarchical levels (Oduguwa and Roy, 2002) and has been used in many fields such as engineering design, transportation, economics and management (Sinha et al., 2014, 2018; Dempe and Zemkoho, 2019; Wu et al., 2021). It is particularly suited for the complex environment requirements involved in the amphibious foil design.

However, most methods require a large number of evaluations, or suffer from local optima. Moreover, these methods are not likely to capture or consider the interactions and trade-offs between geometry and motion parameters, or between different performance objectives. Consequently, sub-optimal solutions may be obtained that fail to fully exploit the coupling effects between geometry and motion (Wang et al., 2020). Furthermore, most of these methods rely on high-fidelity numerical simulations or experiments, which are computationally expensive or time-consuming.

In this paper, a novel joint multi-objective optimization strategy for amphibious flapping foils is proposed, which leverages a flexible and efficient surrogate model to handle the high-dimensional and noisy data from multiple sources with different levels of fidelity and tasks. The strategy aims to optimize both the geometry and the motion parameters of flapping foils simultaneously, considering multiple performance objectives such as the thrust and the lift. The MOEI, which considers exploration and exploitation as independent objectives (Zhan and Xing, 2020), is combined with the multi-acquisition function (multi-AF) to consist the infill criteria. The multi-AF, proposed in our previous work (Wang et al., 2024), is utilized to balance the convergence of each output. A synthetic test function is adopted to evaluate the prediction accuracy of the strategy. Moreover, a bi-level genetic algorithm framework is applied to conduct configuration optimization for amphibious foils considering multiple motion modalities. The strategy can effectively balance the global and local search, reduce the computational cost, and obtain Pareto-optimal solutions in configuration and motion characteristics.

The rest of this paper is organized as follows. Section 2 introduces the active learning model based on the MMGP, and the infill criteria combined the MOEI and the multi-AF. A joint global optimization, correlation and sensitivity analyses, and a multi-objective configuration optimization along with hydrodynamic analyses are presented in Section 3. Finally, concluding remarks are addressed in Section 4.

2. Materials and methods

2.1. Physical model

Data fusion, which is capable of improving the modeling, optimization and control level, plays a critical and essential role in the study of flapping foil system and the realization of efficient, reliable and flexible flight and propulsion. Basic principles and characteristic parameters of the flapping foil system will be firstly introduced here.

For a single foil as shown in Fig. 1, the geometry parameters include the chord length c, the maximum thickness t, the maximum camber m and the corresponding position p. It is worth noting that t, m and p have been non-dimensionalized by the chord length.

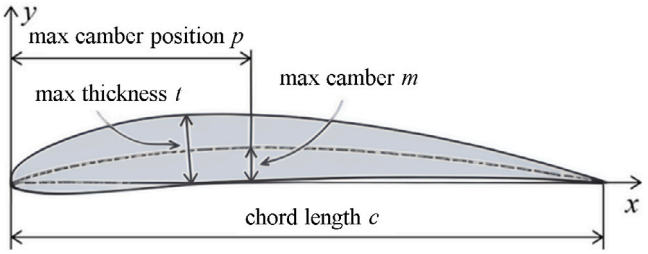

Fig. 1. Schematic diagram of geometry parameters of a foil.

The flapping motion of the foil can be characterized by several parameters. First, the Strouhal number St is defined as follows :

$$\mathrm{St} = \frac{fL}{U} \tag{1}$$

where f is the flapping frequency, U is the free stream velocity, and L is the characteristic length. In present study, the chord length is chosen as the characteristic length. The flapping motion is usually designed as the coupling of two sinusoidal motions with the same period, heaving and pitching,

$$\begin{aligned} y(t) &= y_0 \sin(2\pi f t), \\ \theta(t) &= \theta_0 \sin(2\pi f t + \psi), \end{aligned} \tag{2}$$

where y_0 and θ_0 are the heaving and pitching amplitudes, respectively. ψ stands for the phase angle between the two motions. The flapping motion is shown in Fig. 2.

To describe the performance of the two-dimensional flapping foil, the time-averaged thrust coefficient C_T and lift coefficient C_L are defined, which are derived from the forces in the x and y directions, $F_x(\tau)$ and $F_y(\tau)$, and are further non-dimensionalized. Mathematically, we have :

$$\begin{cases} C_T = \dfrac{1}{\frac{1}{2}\rho U^2 cT} \displaystyle\int_0^T F_x(\tau) d\tau, \\ C_L = \dfrac{1}{\frac{1}{2}\rho U^2 cT} \displaystyle\int_0^T F_y(\tau) d\tau. \end{cases} \tag{3}$$

where T is the flapping period and ρ is the fluid density.

To sum up, there are totally seven parameters for design consideration. Three parameters are related to the foil geometry including the maximum thickness t, the maximum camber m and the corresponding position p, and the other four parameters are related to the flapping motion including the Strouhal number St, the heaving amplitude y_0, the pitching amplitude θ_0 and the phase angle ψ. The time-averaged thrust and lift coefficients, C_T and C_L, are chosen to evaluate the performance of the amphibious foil flapping in water and air.

2.2. Numerical model

In this study, we require a numerical platform that can effectively predict flapping performance. The LilyPad simulation platform, which is based on the boundary data immersion method (BDIM), is applied for the amphibious foil. The BDIM solves the time-dependent Navier–Stokes equations and couples the motion of the body with the surrounding fluid through a kernel function, allowing simulations over the entire domain Weymouth and Yue (2011). Notably, the BDIM method has been previously applied and validated for problems involving flapping foils in studies such as Zheng et al. (2020), Ji et al. (2022) and Sun et al. (2023). The method exhibits second-order convergence and has also garnered validation in a wide range of hydrodynamic simulations (Maertens and Weymouth, 2015; Schlanderer et al., 2017).

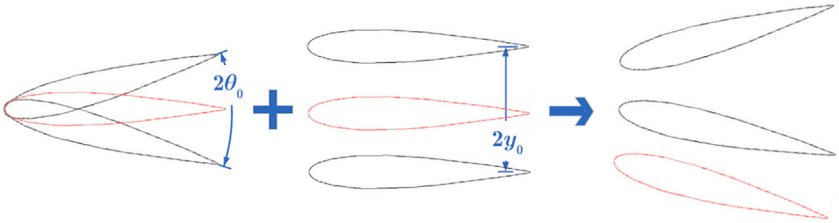

Fig. 2. Schematic diagram of the flapping motion which consists of pitching and heaving.

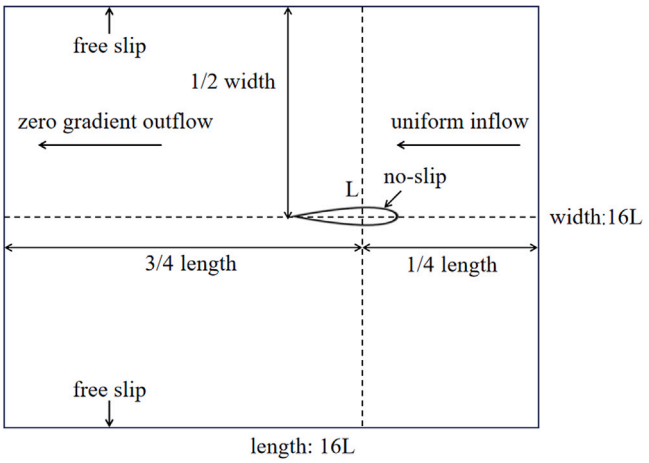

Fig. 3. Sketch of computational domain.

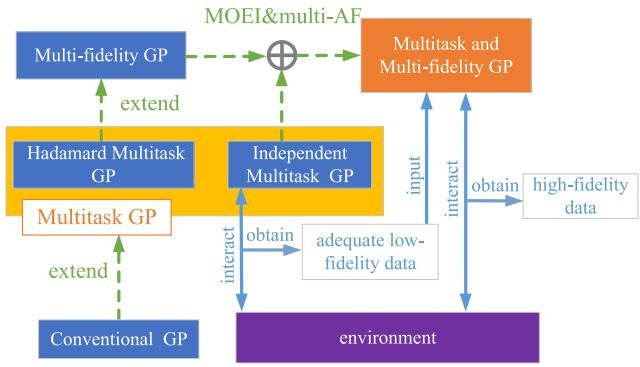

Fig. 4. Framework and workflow of the MMGP. Dashed lines represent framework, while solid lines indicate workflow.

The test case used for validation corresponds to the foil flapping at the Reynolds number $\mathrm{Re} = \rho U c/\mu = 500$ with ρ and μ denoting the density and dynamic viscosity of the fluid. The mesh configuration in this work is a rectangular Cartesian grid, with uniform dense grids used in the field. The domain size is $16L \times 16L$ for high-fidelity simulations and $8L \times 8L$ for low-fidelity simulations. The smaller domain size for low-fidelity simulations is deliberately chosen to reduce the computational time, though this sacrifices a degree of accuracy. A high-fidelity simulation typically takes an average of 8 hour, while a low-fidelity simulation can be completed in a half minute. This allows for rapid results when the high precision is not imperative. Taking the fluid domain for high-fidelity simulations for example, the relative position of the flapping foil center in a state of equilibrium in the fluid domain is shown in Fig. 3. For boundary conditions, the uniform inflow, zero gradient outflow, and free slip at top and bottom are applied. Moreover, a no-slip condition is enforced on the flapping foil. In this study, the grid resolution is represented by the number of grid points per chord length. For a uniform grid, we define $\delta x = \delta y = L/64$ for the high-fidelity simulations and $\delta x = \delta y = L/16$ for the low-fidelity simulations. Detailed validations are presented in Appendix A.

Two main functionalities based on the surrogate model optimization are prediction and optimization. The predictive capability will be assessed through the quantitative analysis of mean absolute error (MAE). The Pareto front demonstrates the optimization results of the Gaussian process model. The use of a Pareto front allows for the visualization of trade-offs in multi-objective optimization problems, thereby offering invaluable insight for identifying the set of potential optimal solutions. This, in conjunction with the MAE assessment, provides a comprehensive evaluation of the model's predictive and optimization performances.

2.3. Active learning model based on MMGP

In order to use a minimum amount of high-fidelity data to accurately predict and optimize multi-objective flapping performance, we propose an innovative MMGP active learning model along with a multi-AF, tailored for flapping multi-objective optimization. The framework and workflow of the MMGP model are shown in Fig. 4.

The MMGP framework integrates the concepts of multi-fidelity GP, drawing inspiration from the Hadamard Multitask GP (Bonilla et al., 2007), and the Independent Multitask GP paired with the multi-AF and MOEI. Both the Hadamard Multitask GP and the Independent Multitask GP are extensions of the Conventional GP(Singletask and Single-fidelity GP). In this context, the multi-fidelity GP evolves from the Hadamard Multitask GP through an adaptation of the index kernel. This index kernel quantifies the covariance between tasks, and uniquely, in the Hadamard Multitask GP, each input aligns with an individual task. The model combines multi-fidelity sub-models and multitask sub-models, which can fully utilize the results of multi-fidelity simulations to effectively handle multi-objective problems. Based on the proposed multi-AF, the candidate samples are selected and then they are automatically simulated to update the MMGP model.

For workflow of the MMGP model, the multitask sub-models engage in real-time interaction with the environment, especially the CFD platform, to acquire adequate low-fidelity data in the initial phase. A Latin hypercube oversampling technique is then employed to secure 50 high-fidelity data samples. These amalgamated data from both high and low fidelity sources serve as the foundation for initializing the MMGP model. As the workflow processes, the MMGP further interacts with the environment to collect high fidelity data, thus initiating the training process.

In the classical active learning framework, various acquisition functions are used to evaluate and quantify the extent to which the candidate points improve the model. However, the common acquisition function can only correspond to one task. In multitask model, how to flexibly balance the improvements of various outputs is crucial to

training effects. In the previous work, the multi-AF is adopted to add more weight to less convergent sub-models. The multi-AF includes a pair of self-adjust coefficients α, and it can be expressed as follows:

$$\delta(\vec{x}) = \alpha \frac{\delta_{ct}(\vec{x})}{\max\left(\delta_{ct}(\vec{x})\right)} + (1-\alpha)\frac{\delta_{cl}(\vec{x})}{\max\left(\delta_{cl}(\vec{x})\right)}, \tag{4}$$

with

$$\begin{cases} \alpha = \dfrac{m}{m+n}, \\ m = \dfrac{\mathrm{MAE}_{ct}}{\max(\hat{f}_{ct}) - \min(\hat{f}_{ct})}, \\ n = \dfrac{\mathrm{MAE}_{cl}}{\max(\hat{f}_{cl}) - \min(\hat{f}_{cl})}, \end{cases} \tag{5}$$

where $\hat{f}_{cl}$ and $\hat{f}_{ct}$ are prediction values of the GP model, MAE_{ct} and MAE_{cl} are average absolute losses of thrust coefficient and lift coefficient that can be estimated from the filling points in the last iteration. It is assumed that there are k points to be infilled in one iteration. Denoting the ith filling point as $\left(\vec{x}_i, f^i\right)$, we have:

$$\begin{cases} \mathrm{MAE}_{ct} = \dfrac{1}{k}\sum_{i=1}^{k}(\hat{f}_{ct}^i - f_{ct}^i) \\ \mathrm{MAE}_{cl} = \dfrac{1}{k}\sum_{i=1}^{k}(\hat{f}_{cl}^i - f_{cl}^i) \end{cases} \tag{6}$$

As for $\delta_{ct}(\vec{x})$ and $\delta_{cl}(\vec{x})$, they can be any acquisition functions in general. The most commonly used acquisition functions include probability of improvement, expected improvement, and upper confidence bound.

2.4. Infill criteria combination of MOEI and multi-AF

The expected improvement is an acquisition function for a single objective that includes two components, exploitation and exploration. It is expressed in the following form:

$$\begin{aligned} \mathrm{EI}(\mathbf{x}) &= \mathrm{E}\left[I(\mathbf{x}) \mid Y(\mathbf{X}) = \mathbf{y}\right], \\ &= \left(y_{min} - \hat{y}(\mathbf{x})\right)\Phi\left(\frac{y_{min} - \hat{y}(\mathbf{x})}{\hat{s}(\mathbf{x})}\right) + \hat{s}(\mathbf{x})\,\phi\left(\frac{y_{min} - \hat{y}(\mathbf{x})}{\hat{s}(\mathbf{x})}\right), \end{aligned} \tag{7}$$

where the first term at the right hand side represents the exploitation part, and the second term considers the uncertainty of exploration. In previous studies, the two components have typically been integrated by the weighted EI method, using a weight factor w to simply balance the exploitation and exploration (Li et al., 2023). Take two outputs for example, the multi-AF can be given as:

$$\mathrm{EI}_{sum} = \alpha \mathrm{EI}_{ct} + \alpha^* \mathrm{EI}_{cl} = \begin{bmatrix} \alpha \\ \alpha^* \end{bmatrix}^{\mathrm{T}} \begin{bmatrix} \mathrm{EI}_{ct} \\ \mathrm{EI}_{cl} \end{bmatrix}, \tag{8}$$

with $\alpha^* = 1 - \alpha$ and

$$\mathrm{EI}_{ct} = w_{ct}\mathrm{EI}_{ct}^{exploit} + w_{ct}^*\mathrm{EI}_{ct}^{explore} = \begin{bmatrix} w_{ct} \\ w_{ct}^* \end{bmatrix}^{\mathrm{T}} \begin{bmatrix} \mathrm{EI}_{ct}^{exploit} \\ \mathrm{EI}_{ct}^{explore} \end{bmatrix}, \tag{9a}$$

$$\mathrm{EI}_{cl} = w_{cl}\mathrm{EI}_{cl}^{exploit} + w_{cl}^*\mathrm{EI}_{cl}^{explore} = \begin{bmatrix} w_{cl} \\ w_{cl}^* \end{bmatrix}^{\mathrm{T}} \begin{bmatrix} \mathrm{EI}_{cl}^{exploit} \\ \mathrm{EI}_{cl}^{explore} \end{bmatrix}, \tag{9b}$$

where $w_{ct}^* = 1 - w_{ct}$ and $w_{cl}^* = 1 - w_{cl}$ are defined to make the expressions compact. Equivalently, we have:

$$\mathrm{EI}_{sum} = \mathrm{EI}^{exploit} + \mathrm{EI}^{explore}, \tag{10}$$

with $\mathrm{EI}^{exploit}$ representing the total exploitation,

$$\mathrm{EI}^{exploit} = \alpha w_{ct}\mathrm{EI}_{ct}^{exploit} + \alpha^* w_{cl}\mathrm{EI}_{cl}^{exploit} = \begin{bmatrix} \alpha \\ \alpha^* \end{bmatrix}^{\mathrm{T}} \begin{bmatrix} w_{ct} & 0 \\ 0 & w_{cl} \end{bmatrix} \begin{bmatrix} \mathrm{EI}_{ct}^{exploit} \\ \mathrm{EI}_{cl}^{exploit} \end{bmatrix}, \tag{11a}$$

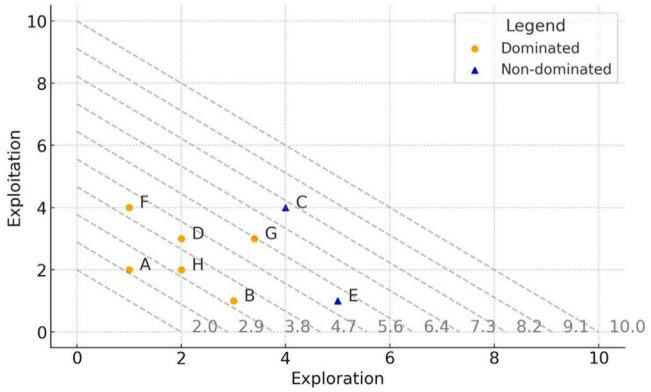

Fig. 5. The total exploration and exploitation components during the training process. The triangular points (blue online) denote the Pareto front.

and $\mathrm{EI}^{explore}$ representing the total exploration,

$$\mathrm{EI}^{explore} = \alpha w_{ct}^*\mathrm{EI}_{ct}^{explore} + \alpha^* w_{cl}^*\mathrm{EI}_{cl}^{explore} = \begin{bmatrix} \alpha \\ \alpha^* \end{bmatrix}^{\mathrm{T}} \begin{bmatrix} w_{ct}^* & 0 \\ 0 & w_{cl}^* \end{bmatrix} \begin{bmatrix} \mathrm{EI}_{ct}^{explore} \\ \mathrm{EI}_{cl}^{explore} \end{bmatrix}. \tag{11b}$$

Though some studies have employed varying weights to address trade-offs between different objectives (Arias-Montano et al., 2012), this method essentially maps candidate points onto isolines in the total exploration–exploitation Pareto front plane, as illustrated in Fig. 5. Comparing with the actual Pareto front, the above mapping method may lead to sub-optimal selections. For example, the weighted EI method is likely to select points C and G, which are actually inferior to the non-dominated solutions C and E.

Therefore, the MOEI is further fused with the multi-AF in this study to treat the total exploration and exploitation components as two objectives, as shown in Fig. 6. Points on the Pareto front are selected in each iteration as the infill criteria of the model.

3. Results and discussions

3.1. Verification of MOEI

Though the superiority of MOEI has been previously established in Feng et al. (2015), present study focuses on the problem with seven inputs and two outputs to investigate whether the MOEI retains its advantageous performance. To compare the MOEI and the weighted EI method, the ZDT1 test function (Deb et al., 2005; Huband et al., 2006) is utilized as a benchmark due to its flexibility in supporting two outputs and up to thirty inputs or rather decision variables. The ZDT1 test function aims to optimize the following two objectives:

$$\min \quad f(x) = x_1, \tag{12}$$

$$\min \quad g(x) = h(x)\left[1 - \sqrt{\frac{f(x)}{h(x)}}\right], \tag{13}$$

in which,

$$h(x) = 1 + \frac{9}{n-1}\sum_{i=2}^{n} x_i, \quad \text{with} \quad x_i \in [0,1], \tag{14}$$

and $n = 7$ in this study.

The optimization processes are shown in Fig. 7(a) for the weighted EI method and Fig. 7(b) for the MOEI method. During the training process, the MOEI method consistently maintains high predictive accuracy for the second objective $g(x)$, and the predictive accuracy gradually converges for the first objective $f(x)$, reducing the prediction error by

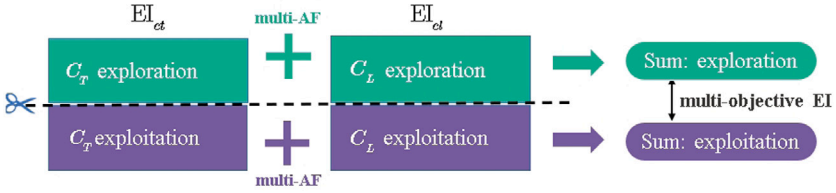

Fig. 6. Infill criteria of the model. The EI of C_T and C_L is partitioned into two components: exploration and exploitation. Through the employment of multi-AF weighted sum, the respective sums of exploration and exploitation are obtained and optimized as two objectives within the multi-objective EI framework.

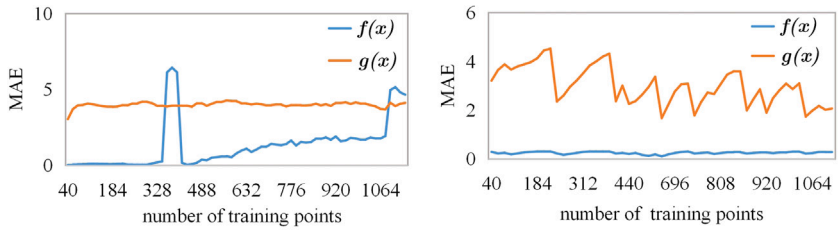

Fig. 7. The MAE prediction accuracy during active learning processes.

50% after 1000 training points. While for the weighted EI method, it is obvious that the prediction error cannot converge for $f(x)$ and cannot significantly reduce for $g(x)$. The failure can be attributed to the poor-quality points selected for the active learning.

3.2. Joint global optimization

A joint online optimization based on the MMGP model is further established, as shown in Fig. 8. A total of 2260 low-fidelity data and 300 high-fidelity data are generated in this study. Both the high-fidelity and low-fidelity data are used to construct the MMGP model, and a randomly sampled test set with 50 high-fidelity data is used to estimate prediction errors. The relative prediction error is measured as the ratio of the MAE to the range of the corresponding output. The MAE of low-fidelity and multi-fidelity are depicted in Fig. 9(a). A low-fidelity model is initially trained by 2260 points, as indicated by the dark and light blue lines. The Latin hypercube sampling is then employed to initialize 50–100 high-fidelity points serving as the foundation for the MMGP model. The Bayesian optimization is subsequently utilized to train the MMGP model till converge, as shown by the red and pink lines. With a foundational set from the low-fidelity model, a rapid convergence is observed in the multi-fidelity model, requiring only 10% of the training points needed for the low-fidelity counterpart.

The self-adjust coefficient α, adjusting to create a balance between the convergence of two outputs, is illustrated in Fig. 9(b) where the blue line is for the low-fidelity and the red line is for the multi-fidelity. Moreover, a trend line is obtained through a 50-window moving average. The increasing trend of the curve indicates the less convergence in the output $\hat{C}_L$ at the early training stage, while the prediction error for the output $\hat{C}_T$ increases in the later stage of training. These observations illustrate the complex dynamics and trade-offs at play during the model training processes.

Based on the training set, the correlations of parameters are evaluated and presented in Fig. 10. These relationships are evidenced by all p-values being less than 0.05, from which it can be concluded that the correlations are indeed significant. For the thrust coefficient C_T, it exhibits significant positive correlations with the Strouhal number St, heaving amplitude y_0, and the maximum thickness t. In contrast, the phase angle ψ has a negative correlation with C_T. For the lift coefficient C_L, it shows strong positive correlations with the Strouhal number St and maximum camber m, while the maximum thickness t

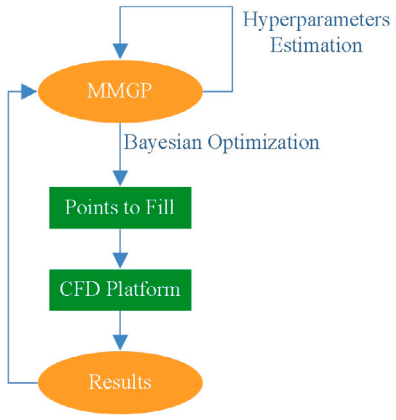

Fig. 8. Framework of joint optimization based on MMGP model.

and maximum camber position p demonstrate a moderate influence and negative correlations with C_L.

Furthermore, the sensitivity of C_L and C_T to variables are also analyzed. The Sobol Global Sensitivity Analysis (GSA) is a variance-based method to understand the importance of each input parameter on a given output (Sobol, 2001). The method calculates two primary metrics, the first-order sensitivity index S and the total-effect sensitivity index ST (Homma and Saltelli, 1996; Saltelli, 2002). The first-order sensitivity index S_i for the ith parameter is given by:

$$S_i = \frac{\mathrm{Var}_{X_i}(\mathbb{E}_{X_{\sim i}}(Y|X_i))}{\mathrm{Var}(Y)}, \tag{15}$$

and the total-effect index ST_i that measures the contribution to the output variance of X_i is defined as:

$$ST_i = 1 - \frac{\mathrm{Var}_{X_{\sim i}}(\mathbb{E}_{X_i}(Y|X_{\sim i}))}{\mathrm{Var}(Y)}. \tag{16}$$

In (15) and (16), Var and $\mathbb{E}$ denote variance and expectation respectively, Y is the output, X_i stands for the ith input parameter and $X_{\sim i}$ denotes all parameters except the ith one. The index S_i indicates the contribution to the output variance of the main effect of input parameter, independently reflects the impact of varying X_i. The index ST_i includes all variance caused by its interactions, of any order, with

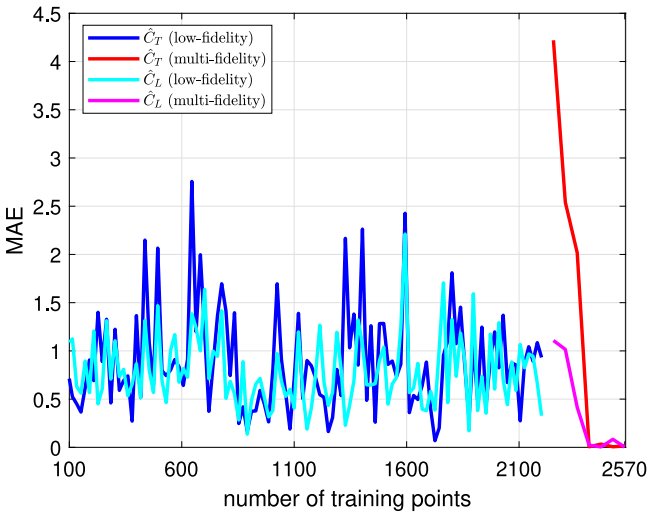

(a) The MAE of the low-fidelity and multi-fidelity.

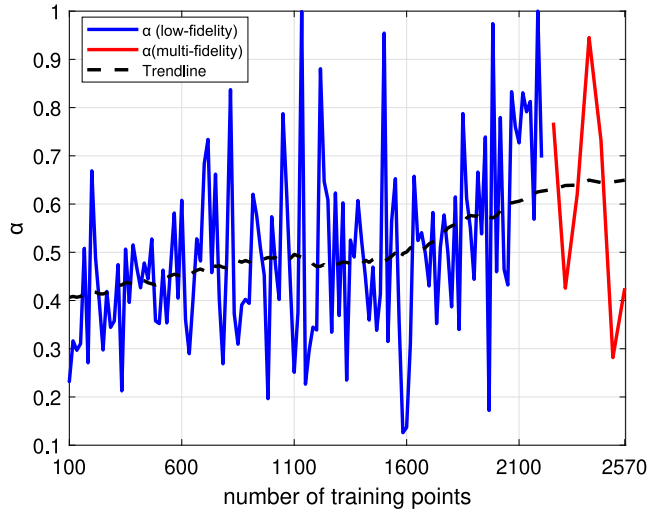

(b) Trend of the self-adjust coefficient α.

Fig. 9. Changes of indicators MAE and α in the training process.

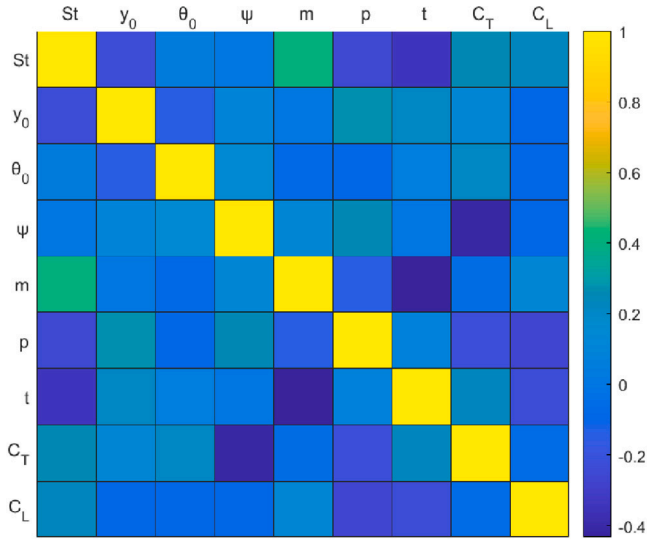

Fig. 10. Correlation matrix about parameters.

Table 1
Relative prediction errors comparison among different models.

Relative prediction error	MMGP + MOEI	Single-fidelity model (Low-fidelity data)	Single-fidelity model (High-fidelity data)
Thrust coefficient C_T	1.96%	2.55%	2.73%
Lift coefficient C_L	2.84%	18.96%	21.46%

any other input variables, reflecting the interaction effect of input parameters.

The results of the Sobol GSA are depicted in Fig. 11 and reveal significant insights into the influence of geometry and motion parameters on C_T and C_L. For the thrust coefficient C_T, the phase angle ψ is the most significant factor with a high $S = 0.3613$ and $ST = 0.6912$. Conversely, the parameter p is the least influential with S closing to zero and $ST = 0.1211$, which suggests that p mostly interacts with other parameters to influence C_T. For the lift coefficient C_L, the heaving amplitude y_0 and the pitching amplitude θ_0 stand out with $S = 0.0891$ and $S = 0.0982$, $ST = 0.4873$ and $ST = 0.5209$ respectively. This suggests that the parameters have substantial and nearly equal influence on C_L. Compared to the motion parameters, the geometry parameters generally exhibit a weaker sensitivity. For instance, in the case of C_T, the most influential geometric parameter is the maximum thickness t with $S = 0.0367$ and $ST = 0.1428$, which are significantly smaller than the corresponding values for the most influential motion parameter ψ.

Overall, it can be concluded that there exists a hierarchy of importance among the seven parameters. For the thrust coefficient C_T, optimizing the phase angle ψ would likely yield the most substantial improvements. For the lift coefficient C_L, attention should be given to both the heaving amplitude y_0 and the pitching amplitude θ_0. Both correlation and sensitivity analyses reveal that motion and geometry parameters considerably influence the performance of the flapping foil. Although motion parameters generally have a greater impact than geometry parameters on both C_T and C_L, the results show that the geometry parameters dominate 22% and 35% of the sum effects on C_T and C_L respectively, suggesting the potential benefit of conducting a joint optimization of motion and geometry parameters to enhance the flapping foil performance.

The correlation analysis of two types of fidelity are also conducted. We normalize all input variables and then select low-fidelity data points that are closest to each high-fidelity point, eliminating those with significant discrepancies. Notably, if the closest low-fidelity point is distant from the high-fidelity point by a Euclidean distance (with a threshold of 0.37) in the parametric space, that high-fidelity point is excluded. Leveraging the familiar pair of the high-fidelity and low-fidelity points, the linear correlations between them are compared, as shown in Fig. 12. It is evident that there is a linear relationship between high-fidelity and low-fidelity results. The linearity appears to be more pronounced for C_T, suggesting that the application of a linear prior formula in the multi-fidelity model (Perdikaris et al., 2015) is effective. The goodness of fit R^2 with definition $R^2 = 1 - (SSE/SST)$ is used as a statistical metric to measure how well the fitted model captures the data (Ross, 2014). SSE is sum of squared errors, representing the sum of squares of the differences between the predicted and observed values of the model. It measures the prediction error of the model. SST is total sum of squares, representing the sum of squares of the difference between the observed values and the mean of the observed data. It represents the overall degree of data variability. The value of R^2 closer to 1 indicates a better fit. In this context, R^2 is 0.7213 for C_T, and is 0.6498 for C_L, indicating the quality of their fits to the respective data.

To illustrate the efficacy of the proposed method, results from the trained model are presented in Table 1. It is essential to note that for the MMGP model, the complete dataset was utilized. In contrast, the single-fidelity model employed either the high-fidelity or the low-fidelity data

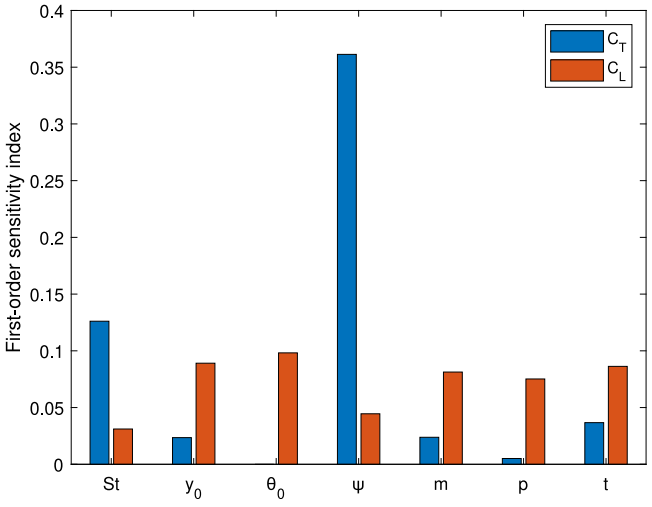

(a) First-order sensitivity.

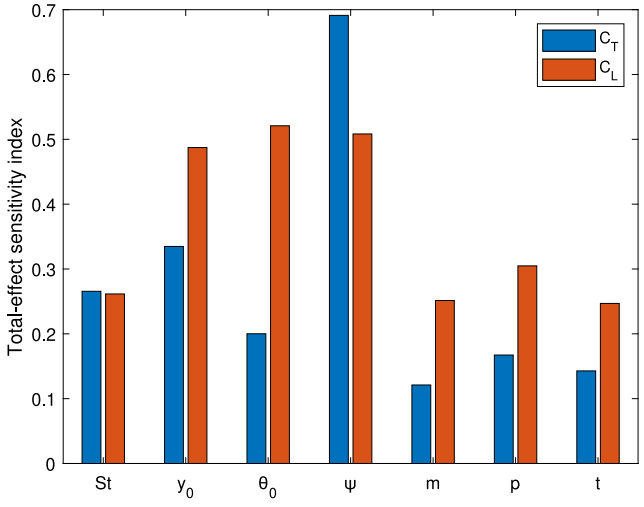

(b) Total-effect sensitivity.

Fig. 11. Sensitivity bar about variables.

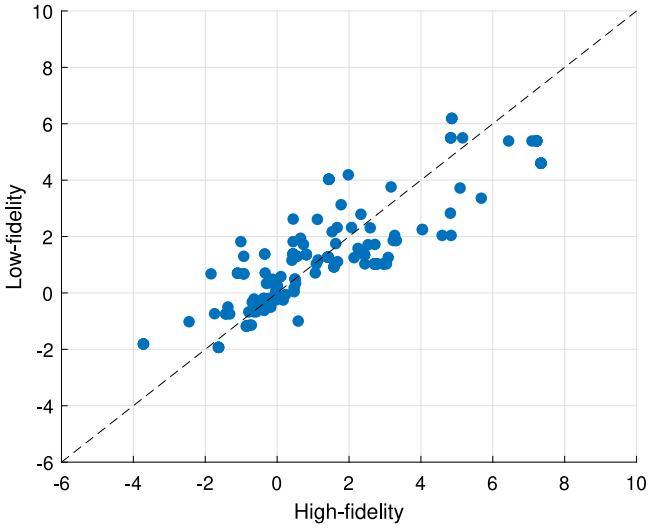

(a) C_T correlation

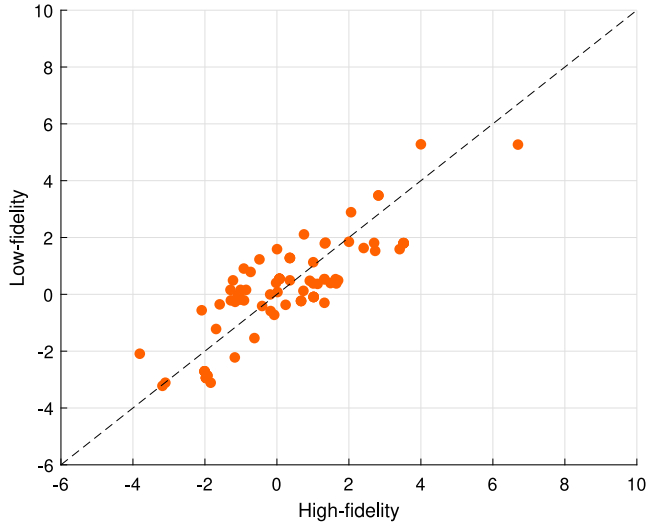

(b) C_L correlation

Fig. 12. Correlations of different fidelities for C_T and C_L.

Table 2
Global multi-objective optimization results.

St	y_0	θ_0	ψ	m	p	t	$\hat{C}_T$	$\hat{C}_L$	C_T	C_L
0.93	0.33	35.12	59.71	4.46%	1.51%	25.50%	4.78	7.31	4.83	7.53
0.92	0.59	21.32	51.10	3.60%	1.17%	34.64%	6.49	7.28	6.54	7.82
0.98	0.59	37.87	5.10	6.35%	0.90%	29.31%	21.68	7.27	21.81	7.49
0.72	0.14	12.57	42.40	8.61%	6.15%	19.74%	1.42	10.98	2.79	2.17

from the comprehensive dataset, depending on the fidelity under consideration. This distinction clearly shows that the prediction accuracy of the MMGP model integrating two fidelities is significantly improved compared with the single-fidelity model, and the prediction error is reduced by 23%–28% for C_T and 85%–87% for C_L as known from Table 1. Subsequently, the well-trained model is optimized through a genetic algorithm, and the Pareto front under two objectives is obtained as shown in Fig. 13.

The points on the Pareto front correspond to different combinations of parameters and objective values, as shown in Table 2 with $\hat{C}_T$, $\hat{C}_L$ denoting predicted values from the MMGP model and C_T, C_L denoting real values from high-fidelity simulations, providing a powerful reference for the design of a flapping foil. A preliminary analysis reveals a commendable congruence between the predicted and real values, thereby affirming the robustness and reliability in capturing the underlying physics of flapping foil dynamics by the MMGP model. Moreover, the data highlights the performance variability attributable to different parameter sets. For instance, certain configurations excel in thrust, with C_T reaching as high as 21.81, whereas others are optimized for lift with C_L being 7.82, respectively. Additionally, the sensitivity of performance metrics to minor variations in parameters like m, p, and t is evident.

3.3. Multi-objective configuration optimization

For the flapping foil, its motion trajectory is easy to change, while the geometry parameters are relatively fixed. In different mission stages, such as swimming in water or flying in air, biological beings adopt different motion trajectories to achieve it (Chin and Lentink,

Table 3
Prediction results of the BiGA.

Point	m	p	t	St	y_0	θ_0	ψ	$\hat{C}_T$	$\hat{C}_L$	C_T	C_L
A	4.46%	1.51%	25.5%	0.93	0.36	35.12	64.4	5.15	–	6.11	–
				0.93	0.36	35.12	59.71	–	9.89	–	7.53
B	6.35%	0.90%	29.31%	0.98	0.59	37.87	5.1	21.65	–	21.81	–
				0.98	0.60	38.27	60.0	–	9.16	–	9.25

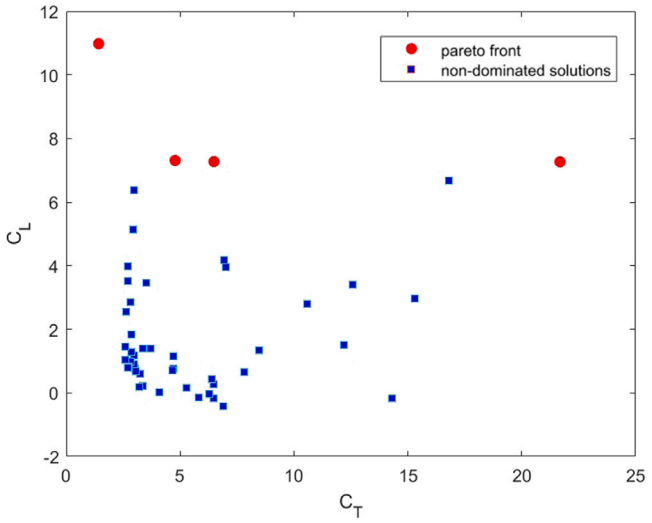

Fig. 13. Pareto front (circle points, red online) obtained from optimization based on MMGP model.

2016). Therefore, it is meaningful to design two different motion trajectories for a same foil to achieve high lift and large thrust modes. Based on the above well-trained MMGP model, a BiGA framework is further designed to achieve this goal. As shown in Fig. 14, the outer layer GA1 is responsible for selecting foil configurations, the last pop of global optimization is recommended to be used as the initial pop of GA1 to speed up the convergence. For each configuration, the inner layer GA2 performs trajectory optimization based on the MMGP model, with both thrust and lift being positive as boundary conditions, and two groups of motion parameters with the maximum thrust and the maximum lift are used as response values of GA1 input. Therefore, an optimization framework is constructed in which three geometry parameters serve as inputs, and the optimal thrust and lift of the trajectories serve as outputs.

The optimization results, encapsulated across multiple generations and graphically represented in Fig. 15, stand as a testament to the dynamic and adaptable nature of the BiGA framework. To expedite convergence, the high-performance points in the dataset are utilized as the initial population. The Table 3 distinctly showcases the predicted ($\hat{C}_T$ and $\hat{C}_L$) and real (C_T and C_L) performance metrics of non-dominated solutions (point A and B) in Fig. 15. The results demonstrate that flexible switching between different motion modes for the same foil allows the corresponding C_T and C_L to surpass the global optimum as shown in Table 2. For instance, with parameters $m = 6.35\%$, $p = 0.90\%$, and $t = 29.31\%$, the foil achieves a notable real thrust of 21.81 or a lift of 9.25. Compared with point $C_T = 21.81$ and $C_L = 7.49$ in Table 2, a equivalent performance can be maintained by point B on one objective, while a 25% enhancement at least is observed on the other. It further shows the efficacy of the proposed method in navigating the complex design space, ultimately benefiting the design of amphibious foils by delivering optimized performance metrics. Moreover, an in-depth hydrodynamic analysis has also been carried out to understand the physical mechanism of high thrust and high lift from the view of the vorticity field. Detailed discussions are presented in Appendix B.

4. Concluding remarks

Leveraging the synergy of the multitask and multi-fidelity Gaussian process model and the bi-level genetic algorithm optimization framework, this study proposes a robust methodology for the optimization of the flapping foil which is widely used in the bio-inspired equipment. The core contributions can be summarized as follows:

1. We extend the capabilities of the MMGP model by integrating the MOEI acquisition function. Through a rigorous test on the ZDT1 function, we demonstrate the superior predictive accuracy of this acquisition function over traditional fixed-coefficient methods. This is of importance for its application in more complex optimization problems, such as the amphibious foil design.
2. We conduct a comprehensive data-driven analysis to explore the relationship between input–output variables with different fidelities. This understanding makes the design strategy more nuanced and effective. The underlying mechanism of the optimal configuration is also discussed through the fluid dynamic analysis.
3. We propose a bi-level genetic algorithm framework for the joint optimization of amphibious foil trajectory and shape. This not only facilitates global optimization across both geometry and motion parameters but also adapts to multi-objective shape optimization for various motion modal combinations, and provides enhanced performance versatility for amphibious foils in diverse environments.

The numerical results underscore the effectiveness and practical utility of the proposed methodology. The present implementation includes 2260 low-fidelity and 300 high-fidelity data points, enhancing the efficiency of the MMGP model. Owing to a notable linearity between high and low-fidelity data, 0.7213 for C_T and 0.6498 for C_L, a reduction of 23%–28% for C_T, 85%–87% for C_L in prediction errors is obtained comparing with single-fidelity models. The sensitivity of geometry and motion parameters to the output is analyzed, and it is found that the geometry parameters contribute 22% on C_T and 35% on C_L of the sum effects respectively. By deploying the BiGA optimization, the Pareto frontier is obtained. Compared with the global optimum, by flexibly alternating between different motion modalities, a nearly equivalent performance can be maintained on one objective, while a 25% enhancement at least is observed on the other.

Though the proposed method shows promising results, there are still limitations and challenges. The parameterization of the motion is somewhat rough, without taking into account the varying flow fields experienced by the flapping foil or the bio-inspired robot during navigation. For complicated designs, comprehensive training data sets and considerable computational resources are still needed. Looking ahead, we plan to delve into feedback control by harnessing flow field characteristics through clustering. In addition, contemplation of optimal flapping trajectories under varying flow fields is on the horizon, aiming to equip the robot with the capability to adaptively adjust its motion in response to the detected flow field, so as to optimize the performance of acceleration, cruising, and deceleration phases.

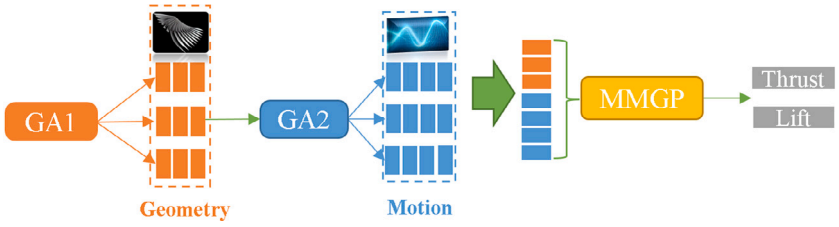

Fig. 14. Optimization framework of BiGA.

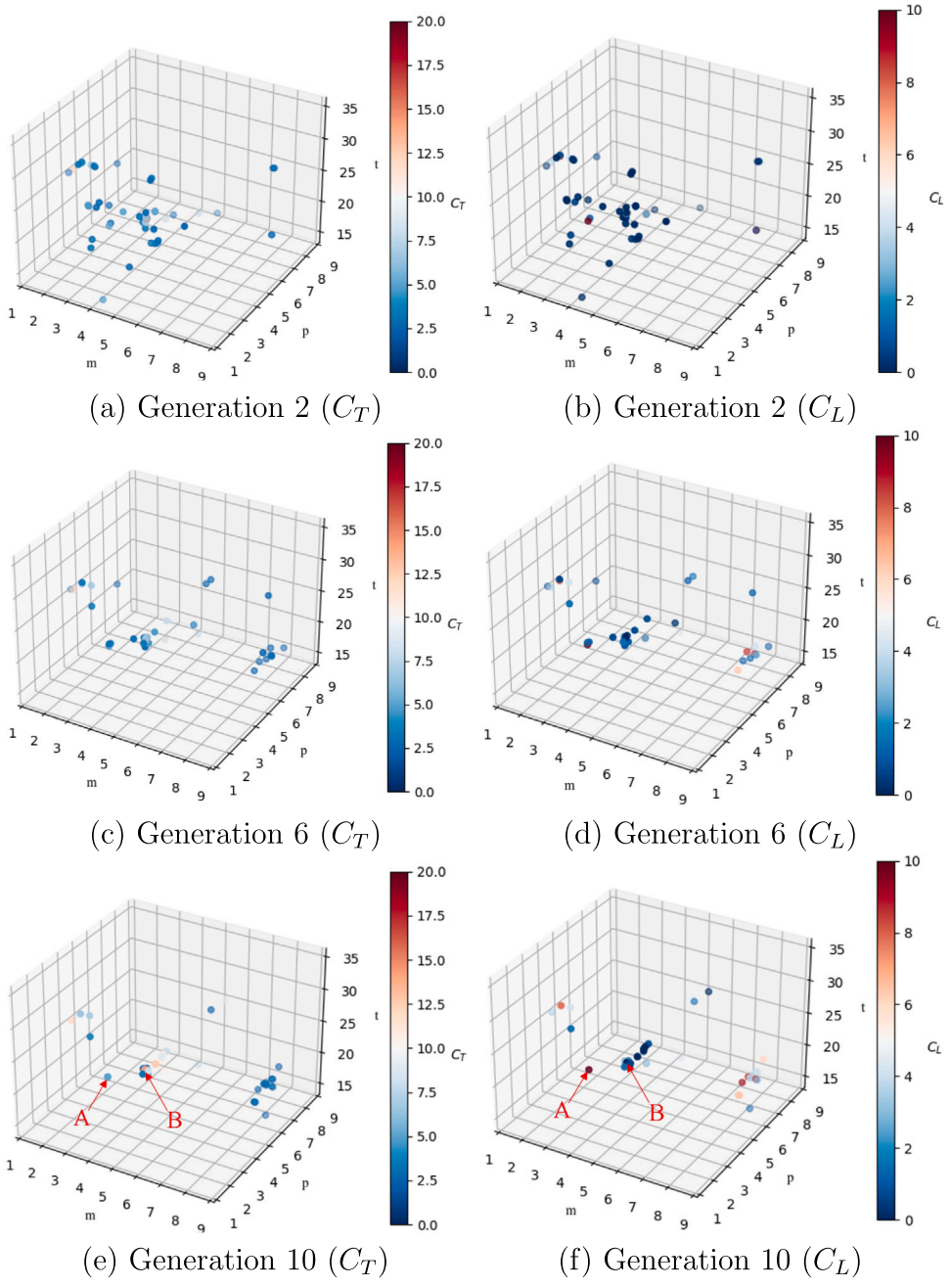

Fig. 15. Evolution of outer layer GA1 over 10 generations for C_T and C_L.

Table A.4
Calculation domain independence analysis.

Resolution	Calculation domain	C_T	C_L
32	$16L \times 16L$	1.048	0.0393
	$32L \times 32L$	1.061	0.0307
48	$16L \times 16L$	1.188	0.0283
	$32L \times 32L$	1.223	0.0231
64	$16L \times 16L$	1.274	0.0242
	$32L \times 32L$	1.275	0.0247
80	$16L \times 16L$	1.271	0.0256
	$32L \times 32L$	1.295	0.0309
	$64L \times 64L$	1.298	0.0303
96	$16L \times 16L$	1.290	0.0273
	$32L \times 32L$	1.297	0.0304
	$64L \times 64L$	1.300	0.0303

CRediT authorship contribution statement

Zhangyuan Wang: Conceptualization, Formal analysis, Methodology, Software, Validation, Visualization, Writing – original draft. **Yuqi Yan:** Formal analysis, Visualization. **Xinyu Zeng:** Visualization. **Ruipeng Li:** Supervision, Writing – review & editing. **Weicheng Cui:** Funding acquisition, Supervision. **Youzhi Liang:** Writing – review & editing. **Dixia Fan:** Conceptualization, Methodology, Resources, Supervision, Writing – review & editing.

Declaration of competing interest

The authors declare that they have no known competing financial interests or personal relationships that could have appeared to influence the work reported in this paper.

Data availability

Data will be made available on request.

Acknowledgments

This research is funded by the National Key Research and Development Program, China (2022YFC2805200), the Key Research and Development Program of Zhejiang Province (2023C03133), the Innovative Research Foundation of Ship General Performance (31422225).

Appendix A. Validations and convergence tests

To demonstrate the effectiveness of the simulation platform, validation cases are configured to align with the settings and motion described in Zheng et al. (2019). The parameters in the simulation is set as follows, $\mathrm{St} = 0.25, y_0 = 1, \theta_0 = 30°, \psi = -\pi/2$ and $\mathrm{Re} = 1100$ for a NACA0015 foil. The accuracy of numerical simulation often depends on the discretization of space and time, so convergence tests are implemented. As mentioned above, the grid resolution is defined as the number of grid points per chord length in this study. A range of grid densities from coarse to fine is simulated to identity the influence on numerical results, or rather on the thrust and lift coefficients of the flapping foil.

The Table A.4 presented in this study displays the impact of resolution on the thrust and lift coefficients across two distinct calculation domains. In each calculation domain, the resolution varies from 32 to 96. It is evident that as the resolution increases, the thrust coefficient exhibits an upward trend, while the lift coefficient experiences a downward trend in both calculation domains. Furthermore, these further investigations revealed that for lower resolutions (64 and less), the calculation domain converges at $16L \times 16L$. However, for higher resolutions (above 64), convergence is achieved at $32L \times 32L$.

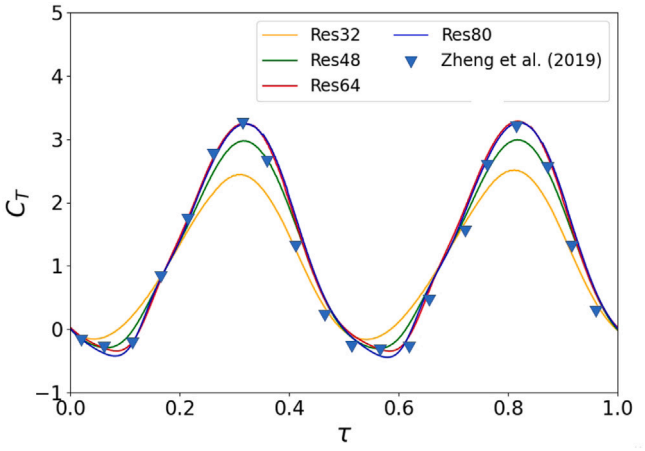

(a) Thrust coefficient

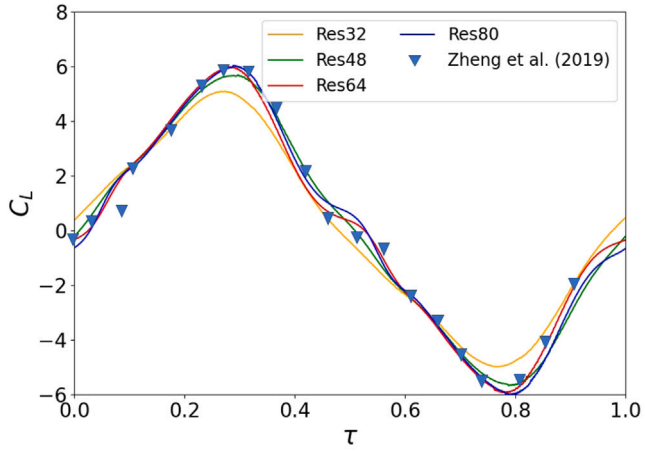

(b) Lift coefficient

Fig. A.16. Comparisons of instantaneous thrust and lift coefficients for different resolution settings with those in Zheng et al. (2019). τ is the dimensionless time that is non-dimensionalized by the flapping period T, and the calculation domain is $16L \times 16L$.

The thrust and lift coefficients under different resolutions are compared as shown in Fig. A.16. The resolution ranges from 32 to 80, and the reference solution is obtained from the aforementioned study (Zheng et al., 2019). It is observed that the thrust coefficient demonstrates a gradual convergence as the resolution increases, with diminishing differences between solutions. Notably, there is virtually no difference between the resolutions of 64 and 80, indicating that a resolution of 64 achieves convergence. Likewise, the lift coefficient also displays a similar convergence behavior, albeit with smaller differences between solutions compared to the thrust coefficient. Based on these findings, a resolution of 64, $16L \times 16L$ is adopted for this study as it strikes a reasonable balance between accuracy and computational efficiency, making it a practical choice for further analysis.

For the temporal resolution, the time step in LilyPad is chosen to be adaptive in order to ensure the explicit stability of convection and diffusion terms. An adaptive time step ($\mathrm{d}t = 1/\max|\mathbf{u}| + 3\nu$) is used to ensure stability. This allows the time step to be automatically adjusted based on the fluid velocity $\mathbf{u}$ and viscosity ν, adapting to different situations. The use of an adaptive time step, along with the Semi-Lagrangian method, is of help to maintain stability while balancing computational efficiency and accuracy (Weymouth, 2015).

Table A.5 shows the thrust coefficient, and lift coefficient values for different time steps. Upon a comparative analysis of these time step sizes, an obvious trend is observed in the changes of thrust coefficient and lift coefficient. For instance, as the time step is reduced from

Table A.5
Time step independence analysis with calculation domain $16L \times 16L$ and resolution of 64. The variable dt represents the default adaptive time step in Lilypad.

Time step	C_T	C_L
1.5dt	1.232	0.0144
dt	1.274	0.0242
0.5dt	1.271	0.0284

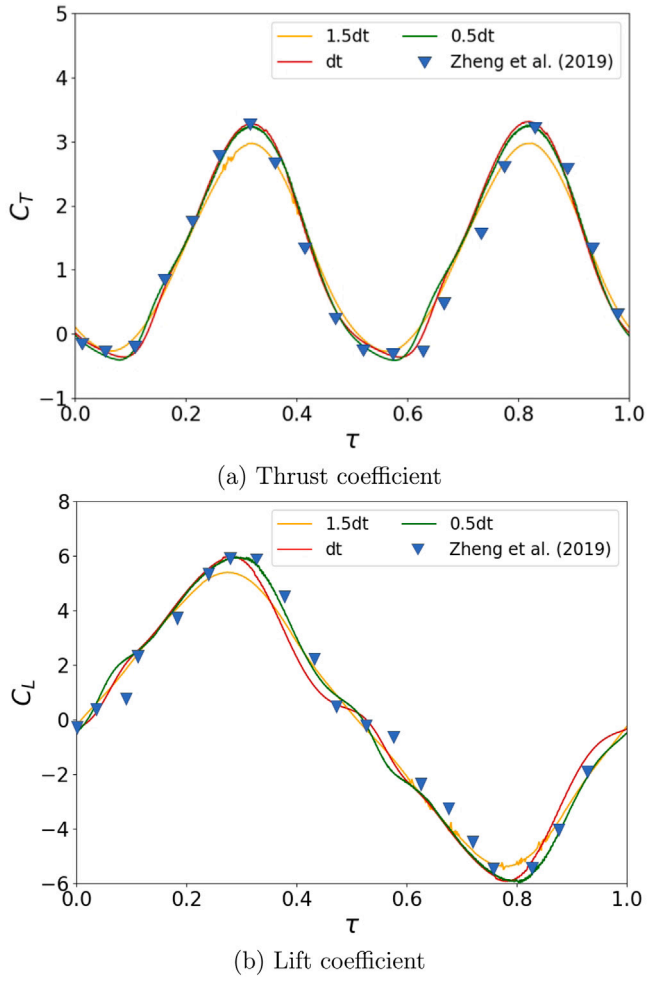

Fig. A.17. Comparisons of instantaneous thrust and lift coefficients for different time settings with those in Zheng et al. (2019). τ is the dimensionless time, the calculation domain is $16L \times 16L$ and the resolution is 64.

1.5dt to dt, the thrust coefficient increases from 1.232 to 1.274, while the lift coefficient decreases from 0.0144 to 0.0242. As the time step is further reduced to 0.5dt, the change of thrust and lift coefficient becomes smaller gradually, with thrust coefficient being 1.271 and lift coefficient being 0.0284. It is known that the thrust and lift coefficients are 1.275 and 0.0291 respectively in Zheng et al. (2019). Fig. A.17 shows the thrust and lift coefficient curves for different time settings, compared with those in Zheng et al. (2019), and a good agreement can be observed for cases of dt and 0.5dt.

Table A.5 and Fig. A.17 indicates that when the time step decreases to dt, the result begins to converge. Further reducing the time step will only result in minimal changes in thrust and lift coefficients, corroborating the efficacy of the chosen adaptive time step dt. This confirms a balance between computational efficiency, accuracy, and stability, eliminating the need for further reduction for the temporal resolution.

Appendix B. Flow field analyses

An in-depth hydrodynamic analysis is carried out for the geometry configuration at Point B in Table 3. As shown in Fig. B.18, the instantaneous thrust and lift curves, along with vorticity fields at crucial instants, are presented for the high thrust mode with $[\mathrm{St}, y_0, \theta_0, \psi] = [0.98, 0.59, 37.87, 5.1]$, and for the high lift mode with $[\mathrm{St}, y_0, \theta_0, \psi] = [0.98, 0.60, 38.27, 60.0]$.

Vorticity fields for the thrust

The left side of Fig. B.18 is depicted for the high thrust mode. As shown in subplot (a), the foil begins its downward locomotion, producing several trailing edge vortexes (TEV) that revolve clockwise above the foil, and the volume of clockwise TEV at the trailing edge increases. At the same time, the angle of attack (AOA) diminishes, and the form drag decreases, resulting in an increasing thrust coefficient. From subplot (b), the thrust generated by the TEV becomes dominant, and the thrust coefficient increases, peaking at $\tau = 0.113$ as illustrated.

As demonstrated in subplots (c-e), the foil continues to flap downward, the AOA decreases, and form drag increases. Although the thrust coefficient decreases, it remains positive. In subplot (e), as the foil starts to flap upward, the form drag gradually decreases, and the thrust coefficient increases. A small counterclockwise rotating vortex, located beyond the leading edge, begins to shed. The shedding of the leading edge vortex (LEV) combines with the TEV, forming a larger TEV, which continues to grow. The thrust generated by this combined TEV leads to a gradual increase in the thrust coefficient, reaching its maximum at $\tau = 0.470$, as depicted in subplots (e-g).

As the TEV moves away from the foil, decreasing the horizontal velocity component of the jet generated by the TEV. As illustrated in subplot (h), the thrust coefficient declines significantly.

Throughout the flapping cycle, the foil leverages the balance of vortex dynamics, primarily the TEV, to generate thrust. During the downward locomotion, the negative thrust arises from the increased form drag due to the AOA. Conversely, the interaction between the foil and the TEV transitions the thrust to positive values. This positive thrust remains dominant for an extended duration, primarily due to the continuous locomotion and the reinforcing behavior of the TEV. The combined effects result in sustained high thrust throughout the flapping period.

Vorticity fields for the lift

As shown in subplot (i), the foil begins its upstroke, causing the fluid to start rotating around the leading edge, creating an initial clockwise vortex. In subplot (j), the clockwise vortex beneath the leading edge hinders the flow of a pair of leading-edge vortices, thereby reducing the flow velocity. This makes a sudden decrease in the fluid pressure difference, consequently decreasing the lift.

In subplot (m)–(n), the foil ends its upstroke. The clockwise vortex reinforces and detaches from the leading edge, moving toward the trailing edge. This temporarily decelerates the fluid below the foil, increasing the pressure difference between the upper and lower sides, and slowing down the lift decreasing.

In subplot (o)–(p), as the AOA continues to increase, several clockwise vortexes start to form above the trailing edge, accelerating the fluid above the foil and increasing the pressure difference between the upper and lower sides, This vortex cancels out the previous counterclockwise vortex, helping to restore lift generation, preparing for the next flapping cycle.

The investigations of the interaction between the flapping foil, vortices, and lift generation emphasize that vortex dynamics and the pressure difference are the key factors affecting lift change. Especially in the process of transition from subplot (j), the forms of a pair of larger vortex structures below the foil may be the main reason for the high lift at the flapping process, consequently increasing the lift.

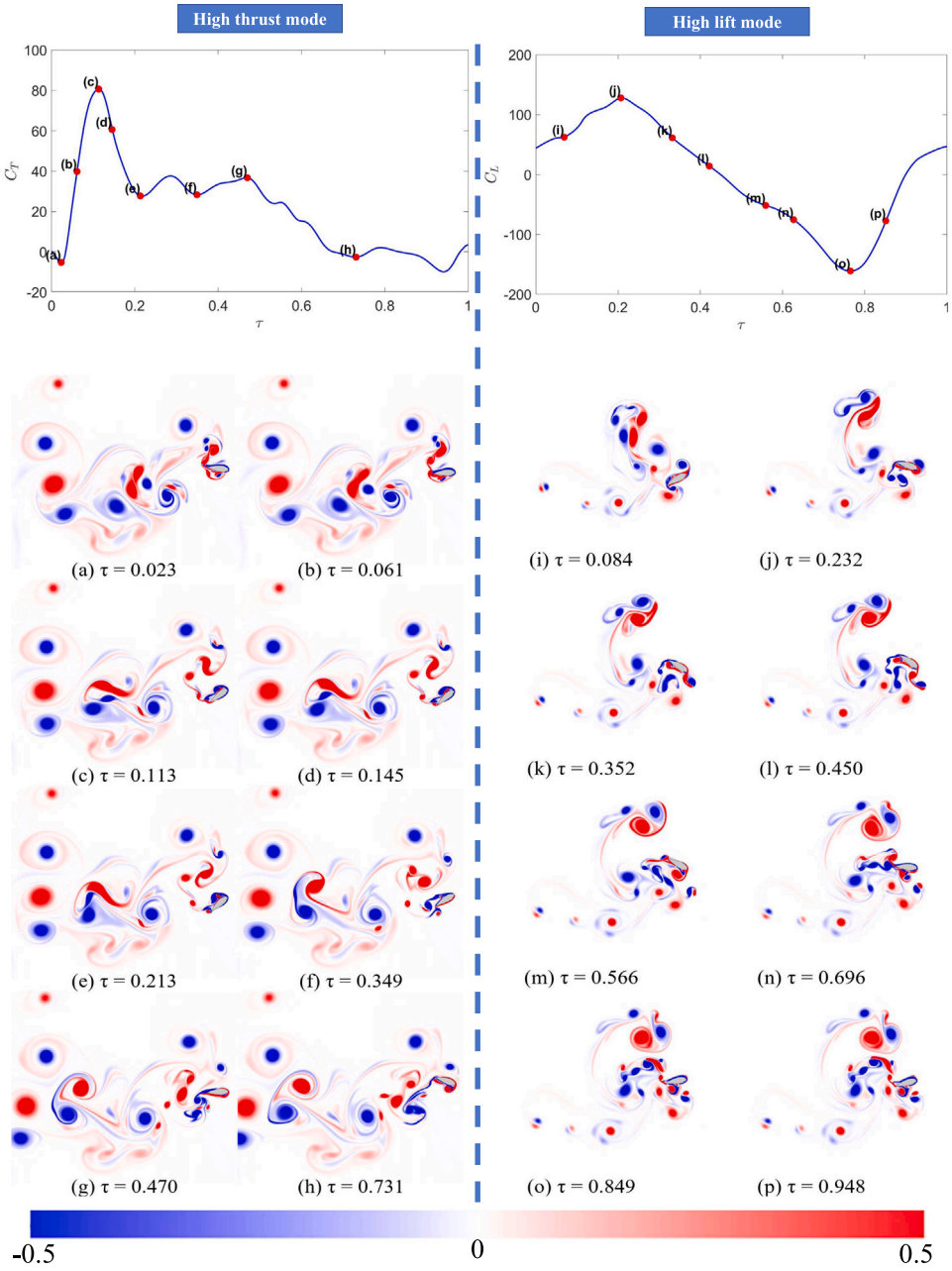

Fig. B.18. Instantaneous lift and thrust curves, along with vorticity fields at crucial instants for the geometry configuration at Point B, left for the high thrust mode and right for the high lift mode. The color bar below represents the vorticity magnitude.

References

Alizadeh, R., Allen, J.K., Mistree, F., 2020. Managing computational complexity using surrogate models: a critical review. Res. Eng. Des. 31 (2), 275–298.

Arias-Montano, A., Coello Coello, C.A., Mezura-Montes, E., 2012. Multi-objective airfoil shape optimization using a multiple-surrogate approach. In: 2012 IEEE Congress on Evolutionary Computation. pp. 1–8.

Bonilla, E.V., Chai, K., Williams, C., 2007. Multi-task Gaussian process prediction. In: Advances in Neural Information Processing Systems. Vol. 20, pp. 153–160.

Chin, D.D., Lentink, D., 2016. Flapping wing aerodynamics: from insects to vertebrates. J. Exp. Biol. 219 (7), 920–932.

Deb, K., Thiele, L., Laumanns, M., Zitzler, E., 2005. Scalable test problems for evolutionary multiobjective optimization. In: Evolutionary Multiobjective Optimization. Springer, pp. 105–145.

Dempe, S., Zemkoho, A. (Eds.), 2019. Bilevel Optimization: Advances and Next Challenges. Springer International Publishing, Cham.

Feng, Z., Zhang, Q., Zhang, Q., Tang, Q., Yang, T., Ma, Y., 2015. A multiobjective optimization based framework to balance the global exploration and local exploitation in expensive optimization. J. Global Optim. 61 (4), 677–694.

Homma, T., Saltelli, A., 1996. Importance measures in global sensitivity analysis of nonlinear models. Reliab. Eng. Syst. Saf. 52 (1), 1–17.

Huband, S., Hingston, P., Barone, L., While, L., 2006. A review of multiobjective test problems and a scalable test problem toolkit. IEEE Trans. Evol. Comput. 10, 477–506.

Ji, T., Jin, F., Xie, F., Zheng, H., Zhang, X., Zheng, Y., 2022. Active learning of tandem flapping wings at optimizing propulsion performance. Phys. Fluids 34 (4), 047117.

Li, F., Gao, L., Shen, W., Garg, A., 2023. Surrogate-assisted multi-objective evolutionary optimization with a multi-offspring method and two infill criteria. Swarm Evol. Comput. 79, 101315.

Li, Z., Wang, Z., 2021. A fireworks algorithm based path planning method for amphibious robot. In: 2021 IEEE International Conference on Real-Time Computing and Robotics. RCAR, IEEE, pp. 1–6.

Licht, S., Wibawa, M., Hover, F.S., Triantafyllou, M.S., 2009. Towards Amphibious Robots: Asymmetric Flapping Foil Motion Underwater and on Land. Technical Report, Massachusetts Institute of Technology.

Maertens, A.P., Weymouth, G.D., 2015. Accurate Cartesian-grid simulations of near-body flows at intermediate Reynolds numbers. Comput. Methods Appl. Mech. Engrg. 283, 106–129.

Oduguwa, V., Roy, R., 2002. Bi-level optimisation using genetic algorithm. In: Proceedings 2002 IEEE International Conference on Artificial Intelligence Systems. ICAIS, pp. 322–327.

Perdikaris, P., Venturi, D., Royset, J.O., Karniadakis, G.E., 2015. Multi-fidelity modelling via recursive co-kriging and Gaussian-Markov random fields. Proc. R. Soc. Lond. Ser. A Math. Phys. Eng. Sci. 471 (2179), 20150018.

Ross, S.M., 2014. Chapter 4 - random variables and expectation. In: Ross, S.M. (Ed.), Introduction to Probability and Statistics for Engineers and Scientists (Fifth Edition), fifth ed. Academic Press, Boston, pp. 89–140.

Saltelli, A., 2002. Making best use of model evaluations to compute sensitivity indices. Comput. Phys. Comm. 145 (2), 280–297.

Schlanderer, S.C., Weymouth, G.D., Sandberg, R.D., 2017. The boundary data immersion method for compressible flows with application to aeroacoustics. J. Comput. Phys. 333, 440–461.

Schouveiler, L., Hover, F.S., Triantafyllou, M.S., 2005. Performance of flapping foil propulsion. J. Fluids Struct. 20 (7), 949–959.

Singh, R.K., Panchal, V., Singh, B.K., 2018. A review on genetic algorithm and its applications. In: 2018 Second International Conference on Green Computing and Internet of Things. ICGCIoT, pp. 376–380.

Sinha, A., Malo, P., Deb, K., 2014. Test problem construction for single-objective bilevel optimization. Evol. Comput. 22 (3), 439–477.

Sinha, A., Malo, P., Deb, K., 2018. A review on bilevel optimization: From classical to evolutionary approaches and applications. IEEE Trans. Evol. Comput. 22 (2), 276–295.

Sobol, I., 2001. Global sensitivity indices for nonlinear mathematical models and their Monte Carlo estimates. Math. Comput. Simulation 55 (1), 271–280, The Second IMACS Seminar on Monte Carlo Methods.

Sun, B., Li, R., Cui, W., Fan, D., Shen, Y., 2023. Gaussian process regression for the side-by-side foil pair. Phys. Fluids 35 (10), 107133.

Sun, B., Li, W., Wang, Z., Zhu, Y., He, Q., Guan, X., Dai, G., Yuan, D., Li, A., Cui, W., Fan, D., 2022. Recent progress in modeling and control of bio-inspired fish robots. J. Mar. Sci. Eng. 10 (6), 773.

Tuncer, I.H., Kaya, M., 2005. Optimization of flapping airfoils for maximum thrust and propulsive efficiency. AIAA J. 43 (11), 2329–2336.

Wang, Z., Yuan, D., Wu, C., Chen, X., Li, R., Cui, W., Fan, D., 2024. Multiobjective optimization for flapping foil hydrodynamics with a multitask and multifidelity approach. Phys. Rev. E 109 (1), 015103.

Wang, Z., Zhang, X., Tian, X., Li, X., 2020. Dual flapping foil system for propulsion and harnessing wave energy: A numerical study. Ocean Eng. 216, 107768.

Weymouth, G.D., 2015. Lily pad: Towards real-time interactive computational fluid dynamics. arXiv:1510.06886.

Weymouth, G.D., Yue, D.K., 2011. Boundary data immersion method for Cartesian-grid simulations of fluid-body interaction problems. J. Comput. Phys. 230 (16), 6233–6247.

Wu, L., Liu, Z., Wei, H.-L., Wang, R., 2021. An efficient bilevel differential evolution algorithm with adaptation of lower level population size and search radius. Memet. Comput. 13 (2), 227–247.

Wu, X., Zhang, X., Tian, X., Li, X., 2020. A review on fluid dynamics of flapping foils. Ocean Eng. 195, 106712.

Zhan, D., Xing, H., 2020. Expected improvement for expensive optimization: a review. J. Global Optim. 78 (3), 507–544.

Zhang, Z., Liang, X., Zhang, S., 2022. Design and optimization of a multimode amphibious robot with propeller-leg. IEEE Trans. Robot. 38 (6), 3807–3820.

Zhang, X., Wu, X., Tian, X., Li, X., 2019. Propulsive performance analysis of underwater flapping multi-foil system based on CFD simulation. In: 2019 IEEE International Conference on Mechatronics and Automation. ICMA, pp. 1744–1749.

Zheng, L., Tang, Y., Guo, S., Ma, Y., Deng, L., 2022. Dynamic analysis and path planning of a turtle-inspired amphibious spherical robot. Micromachines 13 (12), 2130.

Zheng, H., Xie, F., Ji, T., Zhu, Z., Zheng, Y., 2020. Multifidelity kinematic parameter optimization of a flapping airfoil. Phys. Rev. E 101 (1–1), 013107.

Zheng, H., Xie, F., Zheng, Y., Ji, T., Zhu, Z., 2019. Propulsion performance of a two-dimensional flapping airfoil with wake map and dynamic mode decomposition analysis. Phys. Rev. E 99, 063109.